CrystEngComm

PAPER

View Article Online
View Journal | View Issue

Cite this: *CrystEngComm*, 2017, **19**, 3288

Experimental and simulation-based understanding of morphology controlled barium titanate nanoparticles under co-adsorption of surfactants

Zhongyu Sun,†[a] Lei Zhang,†[a] Feng Dang,*[a] Yao Liu,*[a] Zhiying Fei,[b] Qian Shao,[b] Hong Lin,[c] Jiang Guo,[d] Lichen Xiang,[d] Narendranath Yerra[d] and Zhanhu Guo*[d]

Received 9th February 2017,
Accepted 8th May 2017

DOI: 10.1039/c7ce00279c

rsc.li/crystengcomm

Well dispersed single-crystalline $BaTiO_3$ nanoparticles with controlled morphologies were synthesized using a thermohydrolysis route. The nanoparticles were tuned from spherical to cubic upon changing the NaOH concentration under a critical molar ratio of oleic acid to hydrazine. Density functional theory (DFT) and molecular dynamics (MD) calculations indicated that hydrazine molecules adsorbed preferably on the Ti position of the Ti–O terminated surface; meanwhile, oleic acid molecules tended to adsorb on the Ba position of the Ba–O terminated surface. The added hydrazine changed the formation mechanism of $BaTiO_3$ nanoparticles from an *in situ* growth to a dissolution–precipitation growth. Excellent dispersibility in aqueous solution was achieved for the $BaTiO_3$ nanoparticles under the assistance of hydrazine. Meanwhile, a high-quality self-assembled film with a stable dielectric constant of 30 in the frequency range from 0 Hz to 1 MHz was prepared using the well dispersed $BaTiO_3$ nanoparticles, providing a novel low-temperature route for the fabrication of perovskite films.

1. Introduction

Barium titanate ($BaTiO_3$) is widely used as a dielectric material for preparing multilayer ceramic capacitors (MLCCs), embedded capacitors in printed circuit boards, positive temperature coefficient of resistance (PTCR) thermistors, high-performance nanocomposites, and electro-optic devices.[1–7] With the desired miniaturization of developed MLCCs possessing high performance, controlled morphology and good dispersibility on the nanoscale are necessary for using $BaTiO_3$ particles because the crystal face, morphology and size distribution of source nanoparticles significantly influence the electrical properties of $BaTiO_3$ ceramics. Due to successful industrialization of the hydrothermal synthesis of $BaTiO_3$ nanoparticles in aqueous solution, wet methods, such as co-precipitation, hydrothermal and sol–gel have been intensely reported for the preparation of $BaTiO_3$ nanoparticles.[8–11] Surfactants, NaOH concentration, microwave, and sonochemistry are the most commonly used approaches to improve the crystallinity, size distribution and morphology of $BaTiO_3$ nanoparticles.[12–14] Monodispersed $BaTiO_3$ nanoparticles were fabricated by using wet methods.[15–18] For example, an *in situ* growth process was designed to control the morphology of $BaTiO_3$ nanoparticles in aqueous solution.[15] Nucleation and growth of $BaTiO_3$ nanoparticles occurred in the Ti-based hydrous gel that was formed from the hydrolysis of bis(ammonium lactate) titanium dihydroxide (TALH). The $BaTiO_3$ nanocubes with a size of *ca.* 15 nm and their superlattices were obtained through changing the molar ratio of oleic acid (OLA) to *tert*-butylamine. During the process, high concentrations of surfactant and long time (72 h) were necessary, and the morphology control of $BaTiO_3$ nanoparticles was not easy to achieve. Due to the strong coordination effect of OLA molecules with metal ions, a high concentration of OLA limited the dissolution of Ba ions from the Ti–O hydrogel through the hydrolysis of a Ti precursor, and thus *tert*-butylamine had to be added as a co-surfactant to control the adsorption of OLA at the initial formation stage of the $BaTiO_3$ phase.[15] Thus, a novel additive is urgently needed for the morphology control and low cost synthesis of $BaTiO_3$ nanoparticles in this process. Based on this thought, we found that hydrazine was an ideal additive for low cost, high speed and morphology controlled synthesis of $BaTiO_3$ nanoparticles in

[a] *Key Laboratory for Liquid-Solid Structural Evolution and Processing of Materials (Ministry of Education), Shandong University, Jinan 250061, China. E-mail: dangfeng@sdu.edu.cn, iuyao@sdu.edu.cn*
[b] *College of Chemical and Environmental Engineering, Shandong University of Science and Technology, Qingdao 266590, PR China*
[c] *State Key Laboratory of New Ceramic and Fine Processing, Tsinghua University, Beijing, China*
[d] *Integrated Composites Laboratory (ICL), Department of Chemical & Biomolecular Engineering, University of Tennessee, Knoxville, TN 37996, USA. E-mail: uo10@utk.edu*
† These authors contributed equally to this work.

this work. The synthesis design developed in this work shows notable breakthroughs compared with previously reported discoveries.[12–23] First, the minimum concentration of oleic acid needed for morphology control was only one quarter compared to *tert*-butylamine as the surfactant. Second, morphology control of $BaTiO_3$ particles such as cubic, polyhedral and spherical shapes was realized through tuning the NaOH concentration. Furthermore, the growth mechanism of $BaTiO_3$ nanoparticles became a dissolution–precipitation growth process instead of an *in situ* growth process as reported earlier.[15] Although alkylamines and OLA are usually used as the surfactants for the morphology control of nanocrystals, their effects on crystal control have been reported.[19,24–26] However, their detailed roles in the morphology control and interaction with certain crystalline planes have not been well revealed yet.

In this work, we applied density functional theory (DFT) and molecular dynamics (MD) methods to investigate the effect of hydrazine and OLA on the formation mechanism and morphology control of $BaTiO_3$ nanoparticles. DFT calculation is an accurate method in physical analysis on the atomic scale. Meanwhile in some large atomic systems, MD calculations were carried out due to the limitation of computer capacity. For example, Padilla *et al.* calculated the surface energies of $BaTiO_3$ crystal faces by DFT calculation.[27] Yasui *et al.* theoretically studied the formation of $BaTiO_3$ mesocrystals.[28] We found that the favorite adsorption positions of hydrazine and OLA are different. Hydrazine molecules were identified to be the Ti top position on the Ti–O terminated faces. Meanwhile, the favorite adsorption position for oleic acid molecules was identified to be the Ba–O terminated face. Different adsorption characters of hydrazine and oleic acid favored the selective adsorption of OLA on $BaTiO_3$ faces and good dispersion of the $BaTiO_3$ nanoparticles in aqueous solution. Only nanocubes showed the tendency to form superlattices through oriented aggregation in the synthesis process. Owing to high stability and good dispersion in aqueous solution, high quality self-assembled films of $BaTiO_3$ nanocubes were prepared and their dielectric related properties were evaluated.

2. Experimental

2.1 Particle synthesis

In a typical synthesis process, 0.72 mL TALH (TALH, 0.05 mol L^{-1}, Ba : Ti = 1 : 1) was added into 24 mL $Ba(OH)_2$ aqueous solution ($Ba(OH)_2$, 0.05 mol L^{-1}), and then 6 mL NaOH aqueous solution (5 M) was added under mechanical stirring. The initial concentration of NaOH was 1 mol L^{-1}. The aqueous solution was transferred into a 50 mL autoclave, and then hydrazine and oleic acid (OLA) (Ba : OLA : hydrazine = 1 : 2 : 4 in molar ratio) were added into the solution. The sealed autoclave was heated at 220 °C for 48 h, and then cooled down to room temperature. After the synthesis, the precipitate was centrifugally separated and washed twice with ethanol, and then dispersed into deionized water.

2.2 Adsorption energy calculation

Density functional theory (DFT) calculations were performed to investigate the adsorption of hydrazine on $BaTiO_3$ crystal faces, using the CASTEP code aided by the Material Studio graphical front-end interface.[29,30] The generalized gradient approximation (GGA) in the Perdew, Burke, and Ernzerhof (PBE)[31] form was used in energy calculations in different adsorption models. Ultrasoft pseudo potentials were used in the treatment of core electrons.[32] The kinetic cutoff energy was set to be 300 eV and the Monkhorst–Pack special *k*-point mesh was 2 × 2 × 1.

The $BaTiO_3$ surfaces were studied systematically by theoretical calculations.[27,33,34] The (100) face was selected for the DFT calculation because of its highest density of metal ions in the $BaTiO_3$ crystal structure. The (100) face has two typical flat terminations, the Ba–O and Ti–O terminations. In our calculations, a periodic slab with the Ba–O terminated surface containing four Ba–O layers and three Ti–O layers, and a periodic slab with the Ti–O terminated surface containing four Ti–O layers and three Ba–O layers were created, as shown in Fig. 1a and b. The vacuum thickness was set to be 15 Å, in order to avoid the influences of periodic boundary conditions.

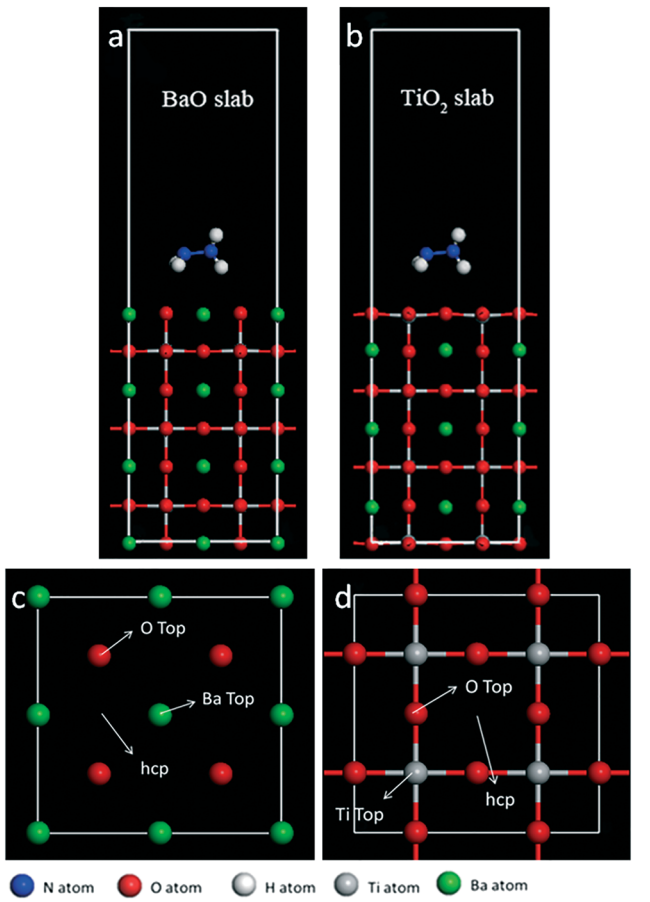

Fig. 1 Slab with (a) the Ba–O terminated surface and (b) the Ti–O terminated surface; initial adsorption positions on (c) the Ba–O terminated surface and (d) the Ti–O terminated surface.

For each model, three typical initial adsorption positions were selected (Fig. 1c and d) to calculate the adsorption energy.

Molecular dynamics (MD) calculations, which are more suitable for the simulations of large molecules, were also performed to identify the adsorption energy of a single oleic acid molecule, using the forcite module aided by the Material Studio graphical front-end interface. The canonical ensemble (NVT) and universal force field[35] were used for the calculations. The temperature was set to be 298 K and the equations of motion were integrated with a 1 fs time step.[36] For each model, the total number of dynamics steps was 200 000.[37]

The models used in MD calculations were constructed as follows. Firstly, a $BaTiO_3$ unit cell was constructed and then optimized by MD calculation. The lattice parameter of the optimized unit cell (4.01 Å) is close to the experimental data (4.00 Å)[27] which suggests that the universal force field can describe our models well. The (100) surface model was created from the unit cell with 7 layers in the z direction (similar to the models used in DFT calculations). The size of the surface was enlarged to 4 × 4 (in fractional units where 1 represents the lattice parameter) along the x and y directions and the vacuum thickness was adjusted to 40 Å to adapt to the large size of an oleic acid molecule. The surface model was then optimized by MD calculations to simulate the reconstruction of the surface atoms. During the MD simulations of oleic acid molecules adsorbed onto the $BaTiO_3$ surface, the optimized surface model was fixed.[37–39]

In both the DFT calculations and the MD calculations, the models of the hydrazine molecules and the oleic acid molecules were constructed according to molecular formula and then optimized by the DFT calculations or MD calculations.[40,41] The number of hydrazine molecules or oleic acid molecules used in the adsorption model is one.

The adsorption energy was calculated using eqn (1):[42,43]

$$E_{ads} = E_{tot}(\text{slab + adsorbate}) - E_{tot}(\text{slab}) - E(\text{adsorbate}) \quad (1)$$

where $E_{tot}(\text{slab} + N_2H_4)$ is the total energy of the optimized slab with a hydrazine molecule adsorbed, $E_{tot}(\text{slab})$ is the total energy of the optimized bare slab and $E(N_2H_4)$ is the energy of a single N_2H_4 molecule.

2.3 Thin film preparation

0.03 mL dispersed $BaTiO_3$ nanocubes (4 mg mL^{-1}) were dropped onto a Pt-coated SiO_2/Si substrate (0.5 × 0.5 cm^2) at room temperature, and then the dispersion was evaporated under UV irradiation (Photo Surface Processor PL21-200, Sen Lights Corp.) in air for 30 min to prepare a particulate film. The top electrodes of Pt, which are 0.4 mm in diameter, were ion-sputtered onto the surface of the self-assembled film for the measurements of the dielectric properties.

2.4 Characterization

The $BaTiO_3$ nanoparticles were characterized by X-ray diffractometry (XRD, D5005HR 3 kw), scanning electron microscopy (SEM, FESEM SU-70), transmission electron microscopy (TEM, JEOL JEM-4010), dynamic light scattering (DLS, ELSZ-1000S), and Fourier transform infrared spectrometry (FT-IR, IRPrestige-21) methods and using a Precision LCR meter (Quadtech 7600 Plus).

3. Results and discussion

Fig. 2 shows the XRD patterns of the $BaTiO_3$ particles synthesized at different NaOH concentrations with Ba : OLA : hydrazine = 1 : 2 : 4 for 48 h. The XRD patterns of all the samples revealed good crystallinity and corresponded to diffraction peaks of the cubic $BaTiO_3$ phase. The weak peaks of the $BaCO_3$ phase at about 24° were identified from the XRD pattern of the particles synthesized at 1.5 mol L^{-1} NaOH. The morphology of $BaTiO_3$ particles can be controlled through the synthesis conditions and this is summarized in Table 1. Fig. 3 shows the TEM images of the particles synthesized at different NaOH concentrations with Ba : OLA : hydrazine = 1 : 2 : 4 for 48 h. The morphology of the $BaTiO_3$ nanoparticles changed with increasing the NaOH concentration. Few $BaTiO_3$ nanocubes with a size of *ca.* 20 nm and unreacted Ti-based gel were observed for the particles synthesized at 1.0 mol L^{-1} NaOH, as shown in Fig. 3a. When the NaOH concentration was increased to 1.2 mol L^{-1}, polyhedral particles with a size of *ca.* 20 nm (Fig. 3b) were mainly observed. For the particles synthesized at 1.5 mol L^{-1} NaOH, nanocubes with round edges were obtained and the particle size ranged from 13 to 18 nm (Fig. 3c). When the NaOH concentration was increased to 2.0 mol L^{-1}, spherical particles with a size of *ca.* 20 nm were obtained (Fig. 3d). These results indicated that the morphology of $BaTiO_3$ particles could be adjusted through changing the NaOH concentration.

Fig. 4 shows the TEM images of the particles synthesized at different NaOH concentrations with Ba : OLA : hydrazine = 1 : 2 : 4 for 72 h. After a long reaction time, only $BaTiO_3$ nanoparticles were identified for the samples synthesized at 1.0 mol L^{-1} NaOH (Fig. 4a). Meanwhile, nanocrystals with an

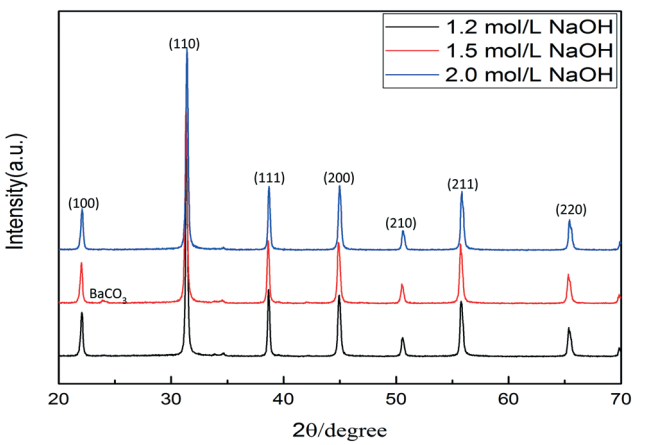

Fig. 2 XRD patterns of the $BaTiO_3$ particles synthesized at different NaOH concentrations with Ba : OLA : hydrazine = 1 : 2 : 4 for 48 h.

Table 1 Relationship of synthesis conditions and morphology types of $BaTiO_3$ nanoparticles

NaOH concentration (mol L^{-1})	Ba : OLA : hydrazine				
	1 : 2 : 0	1 : 2 : 2	1 : 2 : 4	1 : 2 : 8	1 : 0 : 4
1.0	Irregular/amorphous	Irregular	Irregular	—	—
1.2	Irregular/amorphous	Irregular	Polyhedral	—	—
1.5	Cube/amorphous	Cube/irregular	Cube	Cube (large)	Irregular (large)
2.0	Irregular/amorphous	Irregular	Spherical	—	—

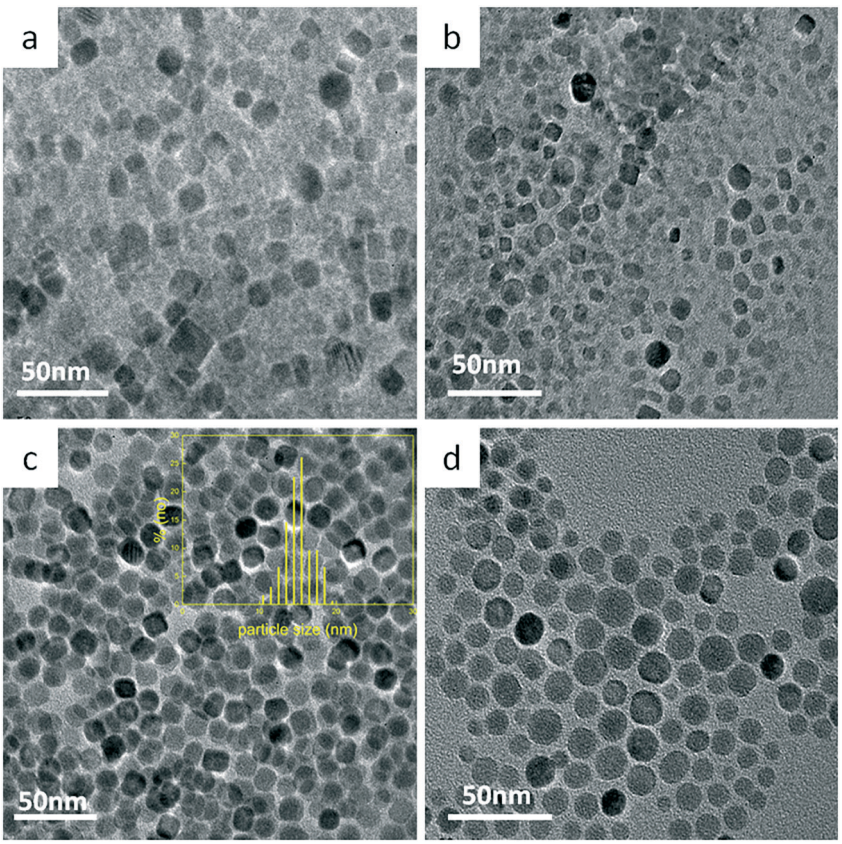

Fig. 3 TEM images of the $BaTiO_3$ synthesized with Ba : OLA : hydrazine = 1 : 2 : 4 for 48 h at NaOH concentrations of: (a) 1.0, (b) 1.2, (c) 1.5, and (d) 2.0 mol L^{-1}.

irregular morphology and a size of *ca.* 10 nm were also observed. The small particles were thought to be obtained from the unreacted Ti-based gel (Fig. 4a). This result indicated that the formation process of $BaTiO_3$ nanoparticles synthesized at low concentrations of NaOH was inhomogeneous and resulted in a broad size distribution. The morphologies of the particles synthesized at high NaOH concentrations did not change largely after a long reaction time (Fig. 4b–d). It is worth noting that large cubes over 150 nm were observed for the particles synthesized at 1.5 mol L^{-1} NaOH for 72 h (Fig. 4e). The ED pattern of the large cubes showed a single crystal structure. Small oriented nanotubes were attached on the surface of the large cubes. Meanwhile, some aggregates of nanocubes were also observed (Fig. 4f). It can be seen that the oriented nanocubes are attached and fused with each other through the (100) face. This result provides strong evidence that large cubic particles were formed through the oriented aggregation of nanocubes. Furthermore, the aggregation of nanoparticles was only identified from the particles with a cubic morphology; no aggregates or large particles were observed for the spherical and polyhedral particles. This result indicates that a cubic morphology has the tendency to form oriented aggregations.

Fig. 5 shows the HRTEM images of nanocubes and spherical particles synthesized at 1.5 and 2 mol L^{-1} NaOH for 72 h. The HRTEM image of the nanocubes showed good crystallinity and round edges. Two sets of (100) and (200) planes were identified from the Fast Fourier Transform (FFT) observed from the [001] direction (Fig. 5a). When the particles were synthesized at a high NaOH concentration (2 mol L^{-1}), the

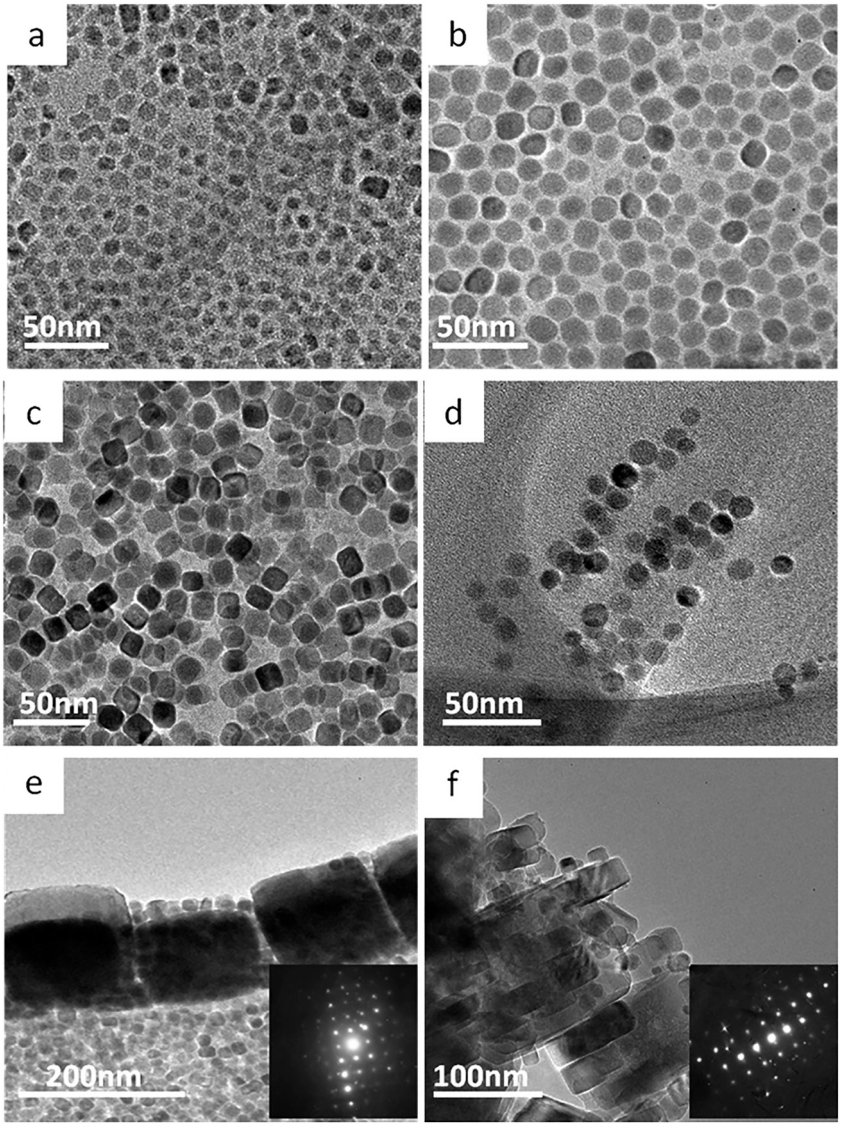

Fig. 4 TEM images of the $BaTiO_3$ synthesized with Ba : OLA : hydrazine = 1 : 2 : 4 for 72 h at the following concentrations of NaOH: (a) 1.0, (b) 1.2, (c, e, f) 1.5, and (d) 2.0 mol L^{-1}.

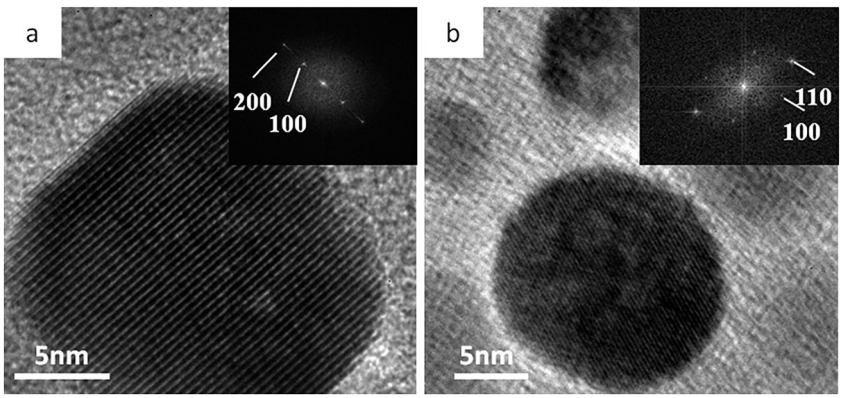

Fig. 5 HRTEM images of nanocubes and nanospheres synthesized at a NaOH concentration of (a) 1.5 and (b) 2 mol L^{-1} for 72 h.

particles evolved into a spherical morphology. The HRTEM image of a spherical particle showed good crystallinity. Two sets of (110) and (100) planes were identified from the FFT (Fig. 5b).

In this study, $BaTiO_3$ nanoparticles with uniform morphology and narrow size distribution were synthesized using a critical molar ratio of OLA to hydrazine. To investigate the effect of OLA and hydrazine on the formation and morphology, $BaTiO_3$ particles were synthesized using different molar ratios of OLA to hydrazine at 200 °C and 1.5 mol L^{-1} NaOH for 72 h, as shown in Fig. 6. Few $BaTiO_3$ nanocubes and an amorphous phase were obtained for the particles synthesized without the addition of hydrazine (Fig. 6a) (Ba : OLA = 1 : 2). When synthesized at a low concentration of hydrazine (Ba : OLA : hydrazine = 1 : 2 : 2), $BaTiO_3$ nanoparticles with an irregular morphology were obtained (Fig. 6b). When synthesized at a high concentration of hydrazine with Ba : OLA : hydrazine = 1 : 2 : 8, ordered arrangements of $BaTiO_3$ nanocubes with a well-defined cubic morphology and sizes ranging from 20 to 30 nm were obtained (Fig. 6c). Large particles over 100 nm with an irregular morphology were obtained for the particles synthesized without the addition of oleic acid (Fig. 6d). These results indicate that the formation of $BaTiO_3$ nanocubes and spheres must be obtained at an appropriate ratio of OLA to hydrazine. Furthermore, hydrazine was important for the formation of the $BaTiO_3$ phase.

To investigate the formation mechanism of $BaTiO_3$ nanoparticles, the formation kinetics of nanocubes synthesized at 1.5 mol L^{-1} NaOH and 220 °C with a molar ratio of Ba : OLA : hydrazine = 1 : 2 : 4 was monitored. Fig. 7 shows the TEM images of the particles synthesized at different reaction time. It can be seen that the formation of nanocubes started from Ti-based hydrous gel, as shown in Fig. 7a. No nuclei or nanocrystals were observed in the Ti-based hydrous gel. After 12 h, $BaTiO_3$ nanoparticles with a size of *ca.* 20 nm and an irregular morphology were obtained (Fig. 7b). No Ti-based hydrous gel was observed at this stage. They have transformed into the $BaTiO_3$ nanocrystals completely. After 24 h, cube-like particles with a size of *ca.* 20 nm were obtained (Fig. 7c). Based on the observation of the particles synthesized for 48 h as shown in Fig. 3c, the $BaTiO_3$ nanoparticles synthesized for 12 h took a long time to transform into a cubic morphology. Based on the observation of the formation kinetics of nanocubes, it can be concluded that the formation of $BaTiO_3$ nanocubes is a dissolution–precipitation process under hydrothermal conditions.[8,10] Hydrazine not only contributed to the morphology control of $BaTiO_3$ nanoparticles but also triggered and accelerated the formation of the $BaTiO_3$ phase.

Furthermore, the application of hydrazine in the synthesis of $BaTiO_3$ nanoparticles can decrease the needed concentration of OLA. Our previous work has synthesized $BaTiO_3$ nanocubes using OLA and *t*-butylamine as the surfactants.[15] It needed a very high concentration of surfactants (Ba : OLA : butylamine = 1 : 8 : 8) to control the morphology of $BaTiO_3$ particles. The formation of $BaTiO_3$ nanocubes was an *in situ* growth mechanism. The $BaTiO_3$ nuclei were formed and grew

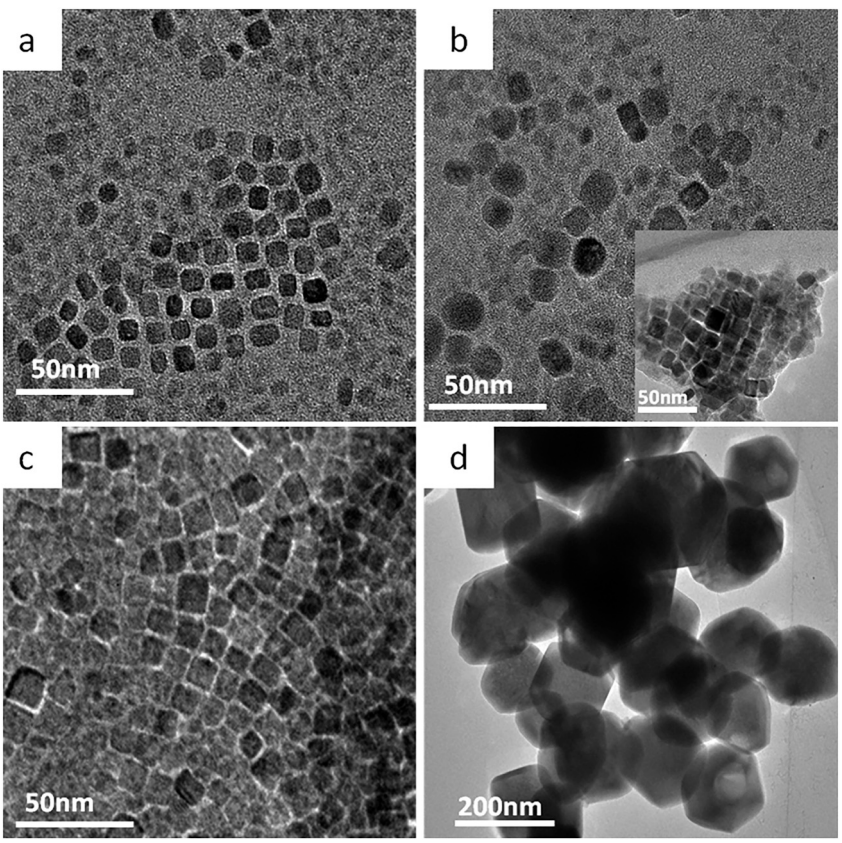

Fig. 6 TEM images of the $BaTiO_3$ synthesized with the following molar ratios of Ba : OLA : hydrazine: (a) 1 : 2 : 0, (b) 1 : 2 : 2, (c) 1 : 2 : 8, and (d) 1 : 0 : 4.

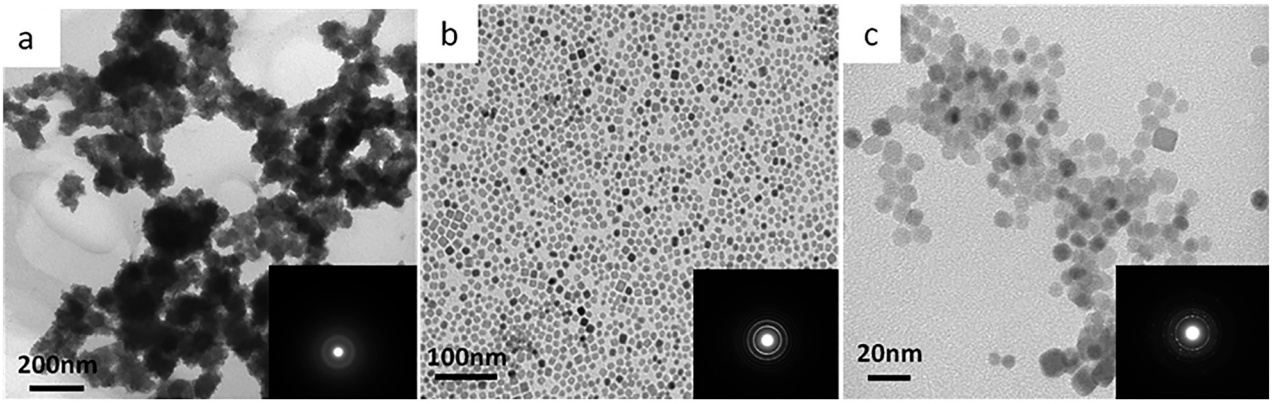

Fig. 7 TEM images of the $BaTiO_3$ synthesized at 220 °C for (a) 2, (b) 12, and (c) 24 h.

from the Ti-based hydrous gel. It took a long time (72 h) for $BaTiO_3$ nuclei to transform into nanocubes through the loss of the Ti-based hydrous gel. In this process, a superlattice of nanocubes could be obtained as an intermediate. It is identified that the formation of $BaTiO_3$ nanocubes was mainly attributed to the selective adsorption of OLA on the (100) face of $BaTiO_3$ with a high atomic density of metal ions.[15,19,24–26] Meanwhile, in the present work, $BaTiO_3$ nanocubes and nanospheres were synthesized at a low concentration of OLA (Ba : OLA : butylamine = 1 : 2 : 4) through the application of hydrazine. Furthermore, the growth mechanism of $BaTiO_3$ nanoparticles changed from an *in situ* growth process into a dissolution–precipitation process through the application of hydrazine with OLA as surfactant during the synthesis process. These results indicate that hydrazine accelerated the formation of the $BaTiO_3$ phase significantly and had an effect on the morphology control of $BaTiO_3$ nanoparticles.

In this work, the influences of hydrazine on the fabrication of $BaTiO_3$ nanoparticles were concluded. The first is the accelerated formation of the $BaTiO_3$ phase. The second is the morphology control of $BaTiO_3$ nanoparticles. For example, Nair *et al.*[44] studied the effect of hydrazine on the self-assembly of CdTe nanocrystals. They found that the zeta potential of OLA stabilized nanoparticles decreased significantly after the addition of hydrazine. Hydrazine could replace the organic ligand adsorbed on the nanoparticle surface. In the dissolution–precipitation process for the formation of $BaTiO_3$ nanoparticles, the Ti monomers dissolved from the hydrous gel form a Ti–O–Ti cross-linked network *via* dehydration at a high concentration of NaOH. The Ba species must break the Ti–O bond and incorporate into the Ti–O cluster, and rearrange to form the $BaTiO_3$ structure.[8,10] The adsorption of OLA will limit the formation of the $BaTiO_3$ phase based on the observation of the results synthesized at different ratios of OLA to hydrazine.[19,24–26] The replacement effect of hydrazine on the adsorbed surfactant molecule can accelerate the dissolution of Ti and Ba species and trigger the formation of the $BaTiO_3$ phase.

Based on the aforementioned results and discussion, the morphology control of $BaTiO_3$ nanocubes could be realized at a proper molar ratio of OLA to hydrazine. In this work, DFT calculations were performed to investigate the adsorption of hydrazine on $BaTiO_3$ faces. The optimized molecular structure of hydrazine and the calculated adsorption energy are shown in Fig. 8. On the Ba–O terminated surface, the largest adsorption energy of −1.92 eV (Fig. 8a) was obtained for the hcp position, which was thought to be the favorite adsorption position. On the Ti–O terminated surface, the favorite adsorption positions were the Ti and O top positions, of which the adsorption energies were −2.94 and −2.96 eV, respectively (Fig. 8e and f), which are significantly larger than that on the Ba–O terminated surface. Meanwhile, it is identified that the hydrazine molecule placed on the O top position moved to the Ti top position for the optimized structure. These results indicate that when a hydrazine molecule gets adsorbed onto the $BaTiO_3$ (100) surface, it prefers to adsorb on the Ti top position on the Ti–O terminated surface.[40,42,43]

The real space view of the electron density difference for a hydrazine molecule adsorbed on the $BaTiO_3$ TiO-terminated surface is shown in Fig. 9a. The purple and yellow parts represent the depletion and accumulation of electron density. It can be seen that there is a slight increase of electron density around the N atom of the hydrazine molecule and a slight decrease of electron density around the Ti atom on the surface, suggesting that there is an interaction between N and Ti atoms. However, the increase and decrease of the electron density are mainly centralized in areas around the N atom and the Ti atom, illustrating the electron transfer is quite weak between the hydrazine molecule and the surface atoms.[45,46] We also calculated the partial density of states (PDOS) of the N atom of the hydrazine molecule and the interacting Ti atom on the surface. The PDOS of N 2s, 2p states of the hydrazine molecule and Ti 3p, 3d, 4s states of the surface are displayed in Fig. 9b. There are only two main resonance peaks at the energy of −3.5 eV and −1.9 eV between the N 2p state and Ti 3p state. The small overlap between the N 2p state and Ti 3p state and the weak strength of resonance peaks also imply that the interaction between N and Ti atoms is quite weak.[45,46] These results indicate that the adsorption of the hydrazine molecule on the $BaTiO_3$ surface is physical adsorption.[47]

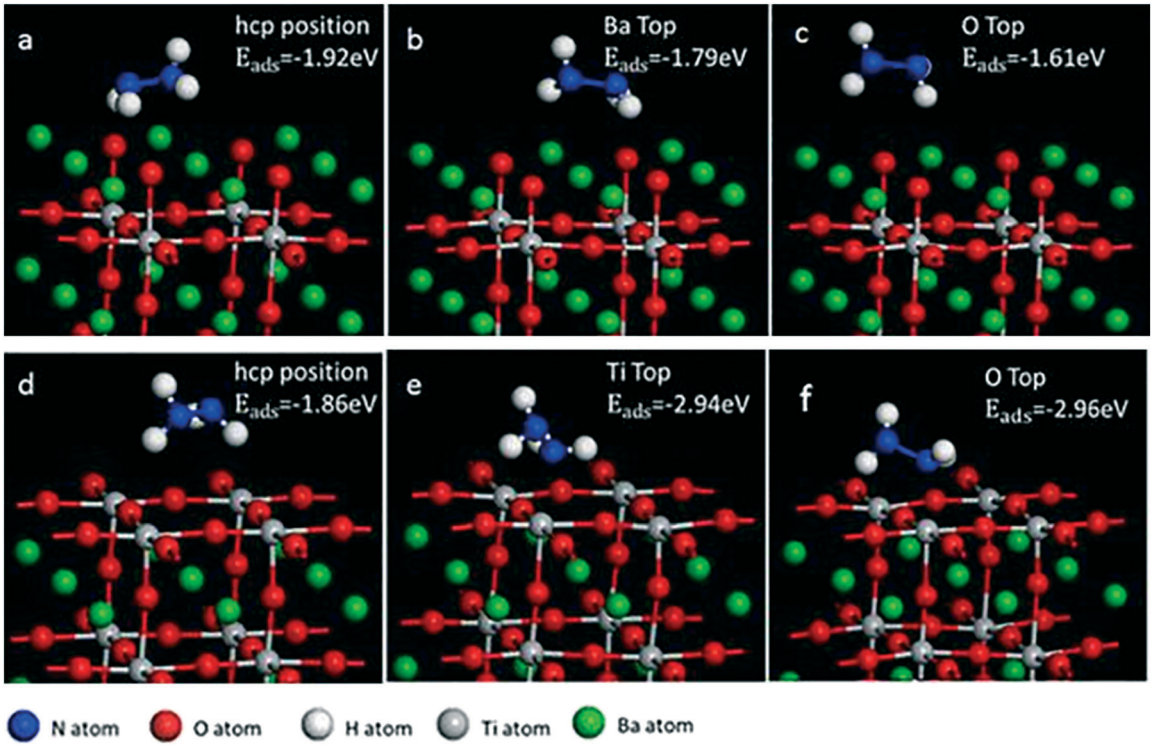

Fig. 8 The optimized structures and calculated adsorption energies of (a–c) the Ba–O terminated surface and (d–f) the Ti–O terminated surface.

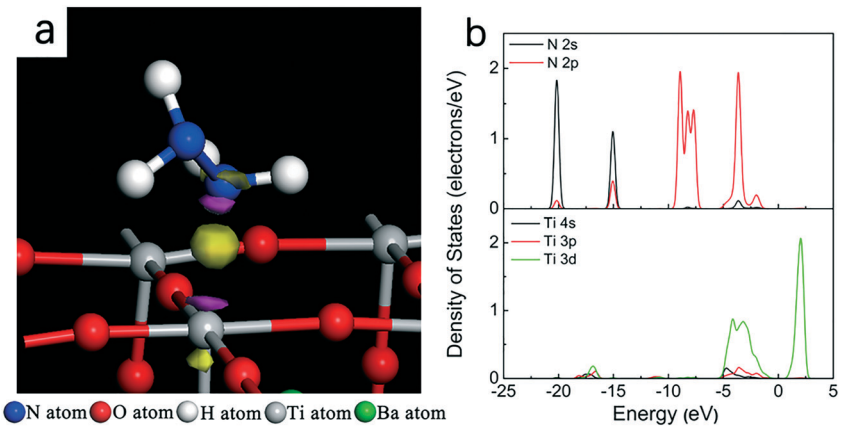

Fig. 9 Real space view of the electron density difference for a hydrazine molecule adsorbed on the $BaTiO_3$TiO-terminated surface (a). Purple and yellow represent the depletion and accumulation of electron density. PDOS of the N atom of the hydrazine molecule and the interacting Ti atom on the surface (b).

The adsorption energy of an OLA molecule on the $BaTiO_3$ surface was also calculated through the molecular dynamics (MD) method. The adsorption energies on Ba–O and Ti–O terminated surfaces are −6.72 eV and −5.92 eV, respectively. This result indicates that the OLA molecule prefers to adsorb on the Ba–O terminated surface. The adsorption of OLA and hydrazine molecules on the $BaTiO_3$ surface are completely different. Our previous work has demonstrated that OLA molecules are chemically adsorbed on the $BaTiO_3$ surface through coordination with metal ions.[15] The present work clarified that the OLA molecules prefer to adsorb on the $BaTiO_3$ surface through coordination with the Ba ions. For the formation of $BaTiO_3$ nanocubes, the (100) face needs to be stabilized through the selective adsorption of OLA. On the other hand, the surface energies of the (100), (110) and (111) faces of $BaTiO_3$ are similar and the (110) face has a higher atom density than the (100) face. Because hydrazine molecules physically adsorb preferably on the Ti–O terminated surface, OLA molecules will mainly adsorb on the $BaTiO_3$ surface through intercalation with Ba ions. Because the Ba ion density on the (100) face is higher than that of other crystal faces, OLA molecules will selectively adsorb on the (100) face

of $BaTiO_3$ under the assistance of hydrazine. It is concluded that the preferred adsorption on the Ti–O terminated surface of hydrazine molecules favors the selective adsorption of OLA molecules on the specific crystal faces of $BaTiO_3$. Because hydrazine mainly physically adsorbs on the $BaTiO_3$ surface, the added hydrazine can accelerate the formation of the $BaTiO_3$ phase in the synthesis process.[40]

The $BaTiO_3$ nanoparticles exhibit excellent dispersibility in aqueous solution (Fig. 10a). The zeta potential of $BaTiO_3$ nanocubes in aqueous solution was −52 mv (pH 10), which was higher than that (−25 mv) of the nanocubes synthesized using *tert*-butylamine as the surfactant. It should be attributed to the physically adsorbed hydrazine. The DLS result of the aqueous dispersion of the nanocubes showed a narrow size distribution. The size of the nanocubes was concentrated from 15 to 20 nm. Due to high dispersibility and stability in aqueous solution, $BaTiO_3$ nanocubes can offer many advantages in the low-temperature processing of ultra thin films on many kinds of substrates, such as Si wafer, metal sheets, plastic, or glass by a variety of solution-based processes including spraying, cast-coating, ink-jet printing, and photolithographic patterning.[19,24,48] Fig. 10b and c show the SEM images of the self-assembled film of $BaTiO_3$ nanocubes using a UV-assisted self-assembly process for the *in situ* decomposition of organic phase on a $Pt/SiO_2/Si$ substrate. The self-assembled film obtained a uniform, continuous, and crack-free surface structure with a thickness of *ca.* 200 nm.

The self-assembled film showed a stable dielectric constant and a dissipation loss in the frequency range from 0 Hz to 1 MHz, only with a slight decrease in capacitance towards high frequency Fig. 10d. The dielectric constant (27–30) is comparable to that reported by Huang *et al.*[48] This further confirms the good homogeneity and quality of the self-assembled film.

4. Conclusions

Sub-20 nm $BaTiO_3$ nanoparticles with controlled morphologies (including nanocubes, spheres and polyhedra) were successfully synthesized with narrow size distribution, good crystallinity and high dispersibility in aqueous solution. Theoretical calculation and kinetics observation indicate that the presence of hydrazine during the synthesis changed the growth mechanism of $BaTiO_3$ nanoparticles and promoted the selective adsorption of OLA on the critical crystal faces. Only $BaTiO_3$ nanocubes showed the tendency towards oriented aggregation. A high quality self-assembled film was prepared at room temperature under UV irradiation using the aqueous solution of $BaTiO_3$ nanocubes. This method has many advantages including mild reaction conditions without high pressure, rapid formation (4 h) and well controlled size and morphology of the product. This work provides a good understanding of the formation mechanism and morphology control of $BaTiO_3$ nanoparticles and demonstrates a methodology for large-scale industrial production of high quality perovskite oxide powders for different applications including thermoelectric power generation,[49] solar

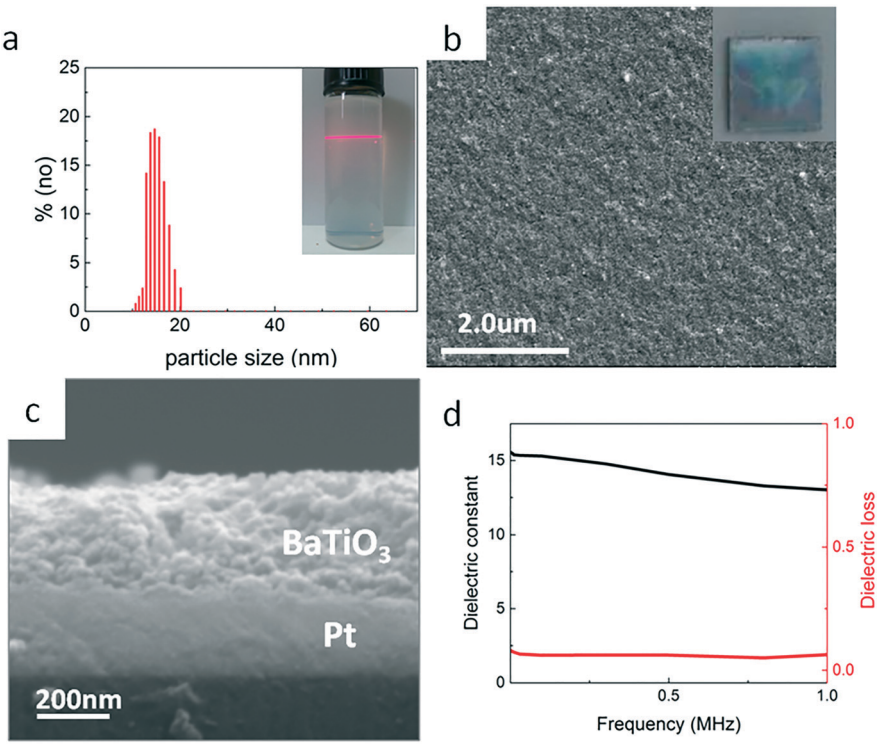

Fig. 10 (a) DLS results and photograph of an aqueous dispersion of $BaTiO_3$ nanocubes, (b and c) SEM images and photograph of the self-assembled film prepared from the aqueous dispersion of $BaTiO_3$ nanocubes, and (d) the dielectric constant and dissipation loss of the self-assembled film.

energy harvesting[50] catalysts[51] and electromagnetic interference shielding.[52]

Acknowledgements

This work was supported by the Natural Science Foundation of Shandong Province (ZR2014EMM001), the State Key Laboratory of New Ceramic and Fine Processing, Tsinghua University (KF201509) and the Qilu program of Shandong University.

References

1 S. Venigalla, Advanced materials and powders digest - Barium titanate ($BaTiO_3$), *Am. Ceram. Soc. Bull.*, 2001, **80**, 63–64.

2 J. Nowotny and M. Rekas, Defect chemistry of $BaTiO_3$, *Solid State Ionics*, 1991, **49**, 135–154.

3 M. Mori, T. Kineri, K. Kadono, T. Sakaguchi, M. Miya, H. Wakabayashi and T. Tsuchiya, Effect of the Atomic Ratio of Ba to Ti on Optical Properties of Gold-Dispersed $BaTiO_3$ Thin Films, *J. Am. Ceram. Soc.*, 1995, **78**, 2391–2394.

4 (*a*) W. Chen, Y. Zheng and B. Wang, Large and Tunable Polar-Toroidal Coupling in Ferroelectric Composite Nanowires toward Superior Electromechanical Responses, *Sci. Rep.*, 2015, **5**, 11165; (*b*) C. Alippi, A unique timely moment for embedding intelligence in applications, *CAAI Trans. Intell. Technol.*, 2016, **1**, 1–3; (*c*) H. Jin, Q. Chen, Z. Chen, Y. Hu and J. Zhang, Multi-LeapMotion sensor based demonstration for robotic refine tabletop object manipulation task, *CAAI Trans. Intell. Technol.*, 2016, **1**, 104–113; (*d*) H. Liu, M. Dong, W. Huang, J. Gao, K. Dai, J. Guo, G. Zheng, C. Liu, C. Shen and Z. Guo, Lightweight Conductive Graphene/Thermoplastic Polyurethane Foams with Ultrahigh Compressibility for Piezoresistive Sensing, *J. Mater. Chem. C*, 2017, **5**, 73–83.

5 (*a*) Z. Yan, Y. Guo, G. Zhang and J. Liu, High-Performance Programmable Memory Devices Based on Co-Doped $BaTiO_3$, *Adv. Mater.*, 2011, **23**, 1351–1355; (*b*) X. Zhang, H. Gao, M. Guo, G. Li, Y. Liu and D. Li, A study on key technologies of unmanned driving, *CAAI Trans. Intell. Technol.*, 2016, **1**, 4–13.

6 Z. M. A. Lum, X. Liang, Y. Pan, R. Zheng and X. Xu, Increasing pixel count of holograms for three-dimensional holographic display by optical scan-tiling, *Opt. Eng.*, 2013, **52**, 015802.

7 (*a*) Z. Tian, X. Wang, S. Lee, K. H. Hur and L. Li, Microstructure Evolution and Dielectric Properties of Ultrafine Grained $BaTiO_3$-Based Ceramics by Two-Step Sintering, *J. Am. Ceram. Soc.*, 2011, **94**, 1119–1124; (*b*) X. Zhang, Q. He, H. Gu, S. Wei and Z. Guo, Polyaniline Stabilized Barium Titanate Nanoparticles Reinforced Epoxy Nanocomposites with High Dielectric Permittivity and Reduced Flammability, *J. Mater. Chem. C*, 2013, **1**, 2886–2899; (*c*) X. Zhang, S. Wei, N. Haldolaarachchige, H. A. Colorado, Z. Luo, D. P. Young and Z. Guo, Magnetoresistive Conductive Polyaniline - Barium Titanate Nanocomposites with Negative Permittivity, *J. Phys. Chem. C*, 2012, **116**, 15731–15740; (*d*) Z. Guo, S. E. Lee, H. Kim, S. Park, H. T. Hahn, A. B. Karki and D. P. Young, *Acta Mater.*, 2009, **57**, 267–277.

8 D. Caruntu, T. Rostamzadeh, T. Costanzo, S. S. Parizi and G. Caruntu, Solvothermal synthesis and controlled self-assembly of monodisperse titanium-based perovskite colloidal nanocrystals, *Nanoscale*, 2015, **7**, 12955–12969.

9 Y. Hao, X. Wang, H. Zhang, L. Guo and L. Li, Sol–gel based synthesis of ultrafine tetragonal $BaTiO_3$, *J. Sol-Gel Sci. Technol.*, 2013, **67**, 182–187.

10 L. Wang, L. Liu, D. Xue, H. Kang and C. Liu, Wet routes of high purity $BaTiO_3$ nanopowders, *J. Alloys Compd.*, 2007, **440**, 78–83.

11 H. Möckel, M. Giersig and F. Willig, Formation of uniform size anatase nanocrystals from bis (ammonium lactato) titanium dihydroxide by thermohydrolysis, *J. Mater. Chem.*, 1999, **9**, 3051–3056.

12 Q. Ma, K. Mimura and K. Kato, Tuning shape of barium titanate nanocubes by combination of oleic acid/tert-butylamine through hydrothermal process, *J. Alloys Compd.*, 2016, **655**, 71–78.

13 M. Hu, V. Kurian, E. A. Payzant, C. J. Rawn and R. Hunt, Wet-chemical synthesis of monodispersed barium titanate particles—hydrothermal conversion of TiO_2 microspheres to nanocrystalline $BaTiO_3$, *Powder Technol.*, 2000, **110**, 2–14.

14 A. Testino, M. Buscaglia, V. Buscaglia, M. Viviani, C. Bottino and P. Nanni, Kinetics and mechanism of aqueous chemical synthesis of $BaTiO_3$ particles, *Chem. Mater.*, 2004, **16**, 1536–1543.

15 F. Dang, K. Mimura, K. Kato, H. Imai, S. Wada, H. Haneda and M. Kuwabara, In situ growth $BaTiO_3$ nanocubes and their superlattice from an aqueous process, *Nanoscale*, 2012, **4**, 1344–1349.

16 F. Dang, K. Kato, H. Imai, S. Wada, H. Haneda and M. Kuwabara, Characteristics of $BaTiO_3$ particles sonochemically synthesized in aqueous solution, *Jpn. J. Appl. Phys.*, 2009, **48**, 09KC02.

17 F. Dang, K. Kato, H. Imai, S. Wada, H. Haneda and M. Kuwabara, A new effect of ultrasonication on the formation of $BaTiO_3$ nanoparticles, *Ultrason. Sonochem.*, 2010, **17**, 310–314.

18 F. Dang, K. Kato, H. Imai, S. Wada, H. Haneda and M. Kuwabara, Oriented aggregation of $BaTiO_3$ nanocrystals and large particles in the ultrasonic-assistant synthesis, *CrystEngComm*, 2010, **12**, 3441–3444.

19 C. Murray, S. Sun, W. Gaschler, H. Doyle, T. Betley and C. Kagan, Colloidal synthesis of nanocrystals and nanocrystal superlattices, *IBM J. Res. Dev.*, 2001, **45**, 47–56.

20 W. Lv, W. He, X. Wang, Y. Niu, H. Cao, J. Dickerson and Z. Wang, Understanding the oriented-attachment growth of nanocrystals from an energy point of view: a review, *Nanoscale*, 2014, **6**, 2531–2547.

21 W. Lv, W. Huo, Y. Niu, Y. Zhu, Y. Xie, X. Guo and W. He, Oriented-attachment dimensionality build-up via van der Waals interaction, *CrystEngComm*, 2015, **17**, 729–733.

22 W. He, An insight into the Coulombic interaction in the dynamic growth of oriented-attachment nanorods, *CrystEngComm*, 2014, **16**, 1439–1442.
23 M. Sushko and K. Rosso, The origin of facet selectivity and alignment in anatase TiO2 nanoparticles in electrolyte solutions: implications for oriented attachment in metal oxides, *Nanoscale*, 2016, **8**, 19714–19725.
24 A. Houtepen, R. Koole, D. Vanmaekelbergh, J. Meeldijk and S. Hickey, The Hidden Role of Acetate in the PbSe Nanocrystal Synthesis, *J. Am. Chem. Soc.*, 2006, **128**, 6792–6793.
25 J. Jin, H. Na, T. Yu, J. Yu, Y. Kim, F. Wu, J. Zhang and T. Hyeon, Generalized and Facile Synthesis of Semiconducting Metal Sulfide Nanocrystals, *J. Am. Chem. Soc.*, 2003, **125**, 11100–11105.
26 S. Mourdikoudis and L. Lizmarzán, Oleylamine in Nanoparticle Synthesis, *Chem. Mater.*, 2013, **25**, 1465–1476.
27 J. Padilla and D. Vanderbilt, Ab initio study of $BaTiO_3$ surfaces, *Phys. Rev. B: Condens. Matter Mater. Phys.*, 1997, **56**, 1625.
28 K. Yasui and K. Kato, Dipole–Dipole Interaction Model for Oriented Attachment of BaTiO3 Nanocrystals: A Route to Mesocrystal Formation, *J. Phys. Chem. C*, 2012, **116**, 319–324.
29 W. Kohn and L. Sham, Self-consistent equations including exchange and correlation effects, *Phys. Rev.*, 1965, **140**, A1133.
30 M. Segall, P. Lindan, M. Probert, C. Pickard, P. Hasnip, S. Clark and M. Payne, First-principles simulation: ideas, illustrations and the CASTEP code, *J. Phys.: Condens. Matter*, 2002, **14**, 2717.
31 J. Perdew, K. Burke and M. Ernzerhof, Generalized gradient approximation made simple, *Phys. Rev. Lett.*, 1996, **77**, 3865.
32 D. Vanderbilt, Soft self-consistent pseudopotentials in a generalized eigenvalue formalism, *Phys. Rev. B: Condens. Matter Mater. Phys.*, 1990, **41**, 7892.
33 R. Eglitis, G. Borstel, E. Heifets, S. Piskunov and E. Kotomin, Ab initio calculations of the $BaTiO_3$ (100) and (110) surfaces, *J. Electroceram.*, 2006, **16**, 289–292.
34 R. Eglitis and D. Vanderbilt, Ab initio calculations of $BaTiO_3$ and $PbTiO_3$ (001) and (011) surface structures, *Phys. Rev. B: Condens. Matter Mater. Phys.*, 2007, **76**, 155439.
35 W. Liu, X. Wang, H. Xu and J. Miller, Lauryl phosphate adsorption in the flotation of Bastnaesite, $(Ce,La)FCO_3$, *J. Colloid Interface Sci.*, 2017, **490**, 825–833.
36 A. Kimmel and P. Sushko, Mechanisms of formation of chemical bonding and defect formation at the a-SiO_2/$BaTiO_3$ interfaces, *J. Phys.: Condens. Matter*, 2015, **27**, 475006.
37 S. Bagheri, A. Shameli, M. Darvishi and G. Fakhrpour, G. Molecular investigation of water adsorption on graphene and graphyne surfaces, *Physica E Low Dimens. Syst. Nanostruct.*, 2017, **90**, 123–130.
38 J. Zeng, W. Shi, G. Sun and S. Chen, Molecular dynamics simulation of the interaction between benzotriazole and its derivatives and Cu_2O crystal, *J. Mol. Liq.*, 2016, **223**, 150–155.
39 M. Nejad, C. Mücksch and H. Urbassek, Insulin adsorption on crystalline SiO_2: comparison between polar and nonpolar surfaces using accelerated molecular-dynamics simulations, *Chem. Phys. Lett.*, 2017, **670**, 77–83.
40 S. Tafreshi, A. Roldan and N. de Leeuw, Hydrazine network on Cu (111) surface: a density functional theory approach, *Surf. Sci.*, 2015, **637**, 140–148.
41 A. Thilagam, K. Kaplun, J. Li and A. Gerson, Interaction of gibbsite with oleic acid: Surface energetics and modelling, *Int. J. Miner. Process.*, 2012, **104**, 24–30.
42 D. He, L. Qiao, A. Volinsky, Y. Bai, M. Wu and W. Chu, Humidity effects on (001) $BaTiO_3$ single crystal surface water adsorption, *Appl. Phys. Lett.*, 2011, **98**, 062905.
43 X. Li, B. Wang, T. Zhang and Y. Su, Water Adsorption and Dissociation on $BaTiO_3$ Single-Crystal Surfaces, *J. Phys. Chem. C*, 2014, **118**, 15910–15918.
44 P. Nair and K. Thomas, Hydrazine-induced room-temperature transformation of CdTe nanoparticles to nanowires, *J. Phys. Chem. Lett.*, 2010, **1**, 2094–2098.
45 Y. Shen, W. Wang, X. Wang, Z. Zhou and W. Fei, First-principles study of CO_2 adsorption on KNTN (001) surfaces, *Appl. Surf. Sci.*, 2014, **308**, 269–274.
46 J. H. Luo, A. M. Hu, X. L. Wang, Y. H. Zhang and Z. S. Li, Adsorption of water on $NaNO_3$ (001) surface from first-principles calculations, *J. Colloid Interface Sci.*, 2013, **393**, 340–346.
47 S. Ayissi, K. Palotás, H. Qin, L. Yang and P. Charpentier, Nanostructural adsorption of vanadium oxide on functionalized graphene: a DFT study, *Phys. Chem. Chem. Phys.*, 2016, **18**, 29208–29217.
48 L. Huang, S. Liu, B. Van Tassell, X. Liu, A. Byro, H. Zhang, E. Leland, D. Akins, D. Steingart and J. Li, Structure and performance of dielectric films based on self-assembled nanocrystals with a high dielectric constant, *Nanotechnology*, 2013, **24**, 415602.
49 Y. Feng, X. Jiang, E. Ghafari, B. Kucukgok, C. Zhang, I. Ferguson and N. Lu, Metal oxides for thermoelectric power generation and beyond, *Adv. Compos. Sci.*, 2017, in press.
50 (*a*) H. He, C. Zhang, T. Liu, Y. Cao, N. Wang and Z. Guo, Thermoelectric-photoelectric composite nanocables induced larger efficiency in dye-sensitized solar cells, *J. Mater. Chem. A*, 2016, **4**, 9362; (*b*) S. R. Aceto, Y. Lu, R. Narayanan, D. R. Hesket, E. K. Wujcik and A. Bose, Hexagonally patterned mixed surfactant-templated room temperature synthesis of titania – lead selenide nanocomposites, *Adv. Compos. Sci.*, 2017, in press.
51 (*a*) Z. Qin, H. Tian, T. Su, H. Ji and Z. Guo, Soft template inducted hydrothermal $BiYO_3$ catalysts for enhanced formic acid formation from the photocatalytic reduction of carbon dioxide, *RSC Adv.*, 2016, **6**, 52665; (*b*) X. Zhou, T. Su, Y. Jiang, Z. Qin, H. Ji and Z. Guo, *Chem. Eng. Sci.*, 2016, **153**, 10.
52 (*a*) J. Guo, H. Song, H. Liu, C. Luo, Y. Ren, T. Ding, M. A. Khan, D. P. Young, X. Liu, X. Zhang, J. Kong and Z. Guo, *J. Mater. Chem. C*, 2017, DOI: 10.1039/C7TC01502J; (*b*) Z. Guo, S. E. Lee, H. Kim, S. Park, H. T. Hahn, A. B. Karki and D. P. Young, Fabrication, characterization and microwave properties of polyurethane nanocomposites reinforced with iron oxide and barium titanate nanoparticles, *Acta Mater.*, 2009, **57**, 267.

